10-21-2013

A Clamped Dual-Ridged Waveguide Measurement System for the Broadband, Nondestructive Characterization of Sheet Materials

Milo W. Hyde IV
Air Force Institute of Technology

Michael J. Havrilla
Air Force Institute of Technology

Recommended Citation

Hyde, M. W., & Havrilla, M. J. (2013). A clamped dual-ridged waveguide measurement system for the broadband, nondestructive characterization of sheet materials. Radio Science, 48(5), 628–637. https://doi.org/10.1002/rds.20044

RADIO SCIENCE, VOL. 48, 628–637, doi:10.1002/rds.20044, 2013

A clamped dual-ridged waveguide measurement system for the broadband, nondestructive characterization of sheet materials

M. W. Hyde IV[1] and M. J. Havrilla[1]

Received 25 September 2012; revised 15 March 2013; accepted 5 June 2013; published 21 October 2013.

[1] A novel two-port probe which uses dual-ridged waveguides for the nondestructive, broadband characterization of sheet materials is presented. The new probe is shown to possess approximately 2 to 3 times the bandwidth of traditional coaxial and rectangular/circular waveguide probe systems while maintaining the structural robustness characteristic of rectangular/circular waveguide probe systems. The theoretical development of the probe is presented, namely, by applying Love's equivalence theorem and enforcing the continuity of transverse fields at the dual-ridged waveguide apertures, a system of coupled magnetic field integral equations is derived. The system of coupled magnetic field integral equations is solved using the method of moments to yield theoretical expressions for the reflection and transmission coefficients. The complex permittivity and permeability of the unknown material under test are then found by minimizing the root-mean-square difference between the theoretical and measured reflection and transmission coefficients. Experimental results of two magnetic absorbing materials are presented to validate the new probe. The probe's sensitivity to measured scattering parameter, sample thickness, and flange-plate thickness errors is also investigated.

Citation: Hyde, M. W., IV, and M. J. Havrilla (2013), A clamped dual-ridged waveguide measurement system for the broadband, nondestructive characterization of sheet materials, *Radio Sci.*, *48*, 628–637, doi:10.1002/rds.20044.

1. Introduction

[2] Radio frequency waveguide probes have been the subject of extensive research for the past half century. Their applications are numerous with nondestructive inspection/evaluation and material characterization applications being the most popular. The most common types of waveguide probes are coaxial [*Folgerø and Tjomsland*, 1996; *Wu et al.*, 2000; *Boybay and Ramahi*, 2011; *Shin and Eom*, 2003; *Olmi et al.*, 2004; *Li and Chen*, 1995; *De Langhe et al.*, 1993; *Baker-Jarvis and Janezic*, 1996; *Bird*, 2004] and rectangular/circular waveguide [*Sanadiki and Mostafavi*, 1991; *Ganchev et al.*, 1992; *Bois et al.*, 1999; *Chang et al.*, 1997; *Maode et al.*, 1998; *Hyde et al.*, 2009b; *Hyde and Havrilla*, 2008; *Tantot et al.*, 1997] probe systems. Coaxial probe systems provide the potential for broadband measurements; however, utilizing them for this purpose can be difficult. In general, small-aperture coaxial probes are most effective when used to characterize high-loss materials. Biological materials are often discussed in the literature, whose loss is driven by water content. On the other hand, large-aperture coaxial probes are required to measure low-loss materials [*De Langhe et al.*, 1993, 1994]. This implies that broadband measurements using coaxial probes are only possible when the material under test (MUT) is known a priori to possess high loss. Rectangular/circular waveguide probes, generally, do not suffer from the coaxial probe "coupling" problem just described and are more structurally robust than their coaxial counterparts; however, they are naturally bandlimited (in some cases, severely).

1.1. One-Port Probe Systems

[3] Both coaxial and rectangular/circular waveguide probe one-port (single) and two-port (dual or clamped) systems have been developed. A great majority of the published waveguide probe research involves one-port probe devices [*Folgerø and Tjomsland*, 1996; *Wu et al.*, 2000; *Boybay and Ramahi*, 2011; *Shin and Eom*, 2003; *Olmi et al.*, 2004; *Li and Chen*, 1995; *De Langhe et al.*, 1993, 1994; *Sanadiki and Mostafavi*, 1991; *Ganchev et al.*, 1992; *Bois et al.*, 1999; *Chang et al.*, 1997; *Maode et al.*, 1998; *Tantot et al.*, 1997]. These systems are very well suited for determining the complex permittivity ε_r of a MUT yet suffer when one desires to fully characterize a material, i.e., determine unambiguously the complex permeability μ_r as well as ε_r, because of the lack of a second independent measurement.

[4] Several one-port-probe techniques have been developed to address this shortcoming by making a second

[1]Department of Electrical and Computer Engineering, Air Force Institute of Technology, Wright-Patterson AFB, Ohio, USA.

Corresponding author: M. W. Hyde IV, Department of Electrical and Computer Engineering, Air Force Institute of Technology, 2950 Hobson Way, Wright-Patterson AFB, Ohio 45433, USA. (milo.hyde@afit.edu)

0048-6604/13/10.1002/rds.20044

"different" reflection S_{11} measurement, most notably, two-thickness method [*Chen et al.*, 2005; *Stewart and Havrilla*, 2006; *Maode et al.*, 1998; *Chang et al.*, 1997], two-layer method [*Baker-Jarvis et al.*, 1994; *Dester et al.*, 2010; *Maode et al.*, 1998; *Tantot et al.*, 1997], frequency-varying method [*Wang et al.*, 1998; *Maode et al.*, 1998], short/free-space-backed method [*Baker-Jarvis et al.*, 1994; *Li and Chen*, 1995; *Tantot et al.*, 1997], and two-iris method [*Dester et al.*, 2012]. However, these techniques typically require some prior knowledge of the MUT (two-thickness method and frequency-varying method), are numerically unstable (two-layer method), are physically difficult to measure (short/free-space-backed method), or require two waveguide probes (two-iris method).

1.2. Two-Port Probe Systems

[5] Two-port probe devices do not suffer from the aforementioned one-port-probe shortcoming because they are able to simultaneously collect two independent measurements, namely, S_{11} and the transmission measurement S_{21}, from which ε_r and μ_r can be unambiguously determined. Two two-port probe geometries currently exist (in both coaxial and rectangular waveguide form)—the dual-probe geometry [*Bird*, 2004; *Hyde et al.*, 2009b] and the clamped-probe geometry [*Baker-Jarvis and Janezic*, 1996; *Hyde and Havrilla*, 2008].

1.3. Overview

[6] In this paper, a novel two-port probe system (clamped-probe geometry) is presented, which uses dual-ridged waveguides (DRWGs) to provide broadband measurements (approximately 2 to 3 times the bandwidth of coaxial and rectangular/circular waveguide probe systems discussed in the literature) while maintaining the structural robustness characteristic of rectangular/circular waveguide probe systems. A schematic of the proposed two-port system (clamped DRWG probe) is shown in Figure 1. The structure consists of two DRWGs attached to Perfect Electric Conductor (PEC) flanges sandwiching the MUT.

[7] The derivation of the theoretical reflection S_{11}^{thy} and transmission S_{21}^{thy} coefficient expressions (theoretical *S*-parameters) necessary to determine ε_r and μ_r of the MUT is presented in section 2. Expressions for the theoretical *S*-parameters are derived using Love's equivalence theorem [*Collin*, 1991; *Peterson et al.*, 1998], in which the DRWG apertures are replaced with equivalent magnetic currents. These currents excite modes in the DRWG and parallel-plate regions of the structure. Expressions for the magnetic field in the MUT are found using the parallel-plate Green's function. Enforcing transverse field continuity at the DRWG apertures produces a system of coupled magnetic field integral equations (MFIEs), which when solved using the method of moments (MoM) [*Harrington*, 1993; *Peterson et al.*, 1998] yields the desired theoretical theoretical *S*-parameters. While the analytical approach is very similar to that of other published waveguide probe research, the complex nature of the DRWG fields greatly complicates the theoretical development and, combined with the substantial gain in measurement bandwidth, represents a significant contribution to waveguide probe research. Note that only the contribution from the dominant DRWG mode is considered here due to the theoretical and computational complexity of the problem.

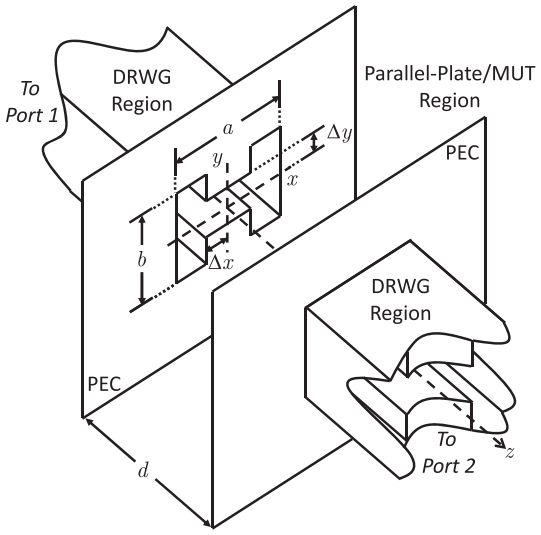

Figure 1. Clamped DRWG probe measurement geometry. The parallel-plate/MUT region is filled with the MUT of unknown permittivity ε and permeability μ; the DRWG regions are free-space-filled.

[8] The system is experimentally validated in section 3, where measurement results of two magnetic absorbing materials obtained using the clamped DRWG probe are compared to results obtained using the traditional Nicolson-Ross-Weir technique [*Nicolson and Ross*, 1970; *Weir*, 1974]. Last, this paper is concluded with a summary of the work presented.

2. Methodology

[9] In this section, theoretical expressions for the reflection and transmission coefficients are derived for the clamped DRWG probe depicted in Figure 1. The form of the transverse fields in the DRWG regions of the apparatus is detailed first, followed by the form of the transverse fields in the parallel-plate/MUT region. A system of coupled MFIEs is then derived by enforcing the continuity of the DRWG and parallel-plate region transverse fields at the DRWG apertures ($z = 0$ and $z = d$ in Figure 1). The solution of the coupled MFIEs via the MoM is then detailed with a final brief discussion on the computation of the impedance matrix elements.

2.1. DRWG Fields

[10] The DRWG field derivation follows the methodology used by *Montgomery* [1971] and *Elliot* [1993] because it is the most applicable approach to the problem of interest. Note that several other methods for analyzing the field behavior in DRWGs exist [*Sun and Balanis*, 1993; *Cho and Eom*, 2001; *Hopfer*, 1955; *Pyle*, 1966; *Utsumi*, 1985; *Helszajn*, 2000].

[11] To arrive at expressions for the fields in the DRWG regions of the clamped DRWG probe, each DRWG subregion (i.e., the gap subregion and the two trough subregions) is expanded in a set of TE^z or TM^z modes [*Collin*, 1991]. Note that since the DRWG dominant mode is a TE^z mode, only the TE^z mode development is relevant here. The mode-matching technique [*Wexler*, 1967] is then used to enforce the continuity of the transverse electric and

magnetic fields at $x = -\Delta x,\ \Delta x$ resulting in a coupled pair of matrix equations:

$$\begin{aligned}
&\alpha_{\tilde{n}}\frac{\tan\left(k_{x\tilde{n}}^{\mathrm{g}}\Delta x\right)-\cot\left(k_{x\tilde{n}}^{\mathrm{g}}\Delta x\right)}{2k_{x\tilde{n}}^{\mathrm{g}}}+\beta_{\tilde{n}}\frac{\tan\left(k_{x\tilde{n}}^{\mathrm{g}}\Delta x\right)+\cot\left(k_{x\tilde{n}}^{\mathrm{g}}\Delta x\right)}{2k_{x\tilde{n}}^{\mathrm{g}}}\\
&\qquad-\sum_{n,m}\alpha_n\frac{\psi_{m,n}\psi_{m,\tilde{n}}\cot\left[k_{xm}^{\mathrm{t}}\left(\frac{a}{2}-\Delta x\right)\right]}{k_{xm}^{\mathrm{t}}\frac{b}{2}(1+\delta_{m,0})\Delta y\left(1+\delta_{\tilde{n},0}\right)}=0\\
&\alpha_{\tilde{n}}\frac{\tan\left(k_{x\tilde{n}}^{\mathrm{g}}\Delta x\right)+\cot\left(k_{x\tilde{n}}^{\mathrm{g}}\Delta x\right)}{2k_{x\tilde{n}}^{\mathrm{g}}}+\beta_{\tilde{n}}\frac{\tan\left(k_{x\tilde{n}}^{\mathrm{g}}\Delta x\right)-\cot\left(k_{x\tilde{n}}^{\mathrm{g}}\Delta x\right)}{2k_{x\tilde{n}}^{\mathrm{g}}}\\
&\qquad-\sum_{n,m}\beta_n\frac{\psi_{m,n}\psi_{m,\tilde{n}}\cot\left[k_{xm}^{\mathrm{t}}\left(\frac{a}{2}-\Delta x\right)\right]}{k_{xm}^{\mathrm{t}}\frac{b}{2}\left(1+\delta_{m,0}\right)\Delta y\left(1+\delta_{\tilde{n},0}\right)}=0
\end{aligned}\quad (1)$$

where

$$\psi_{m,n}=\frac{1}{2}\left(\frac{1}{k_{yn}^{\mathrm{g}}-k_{ym}^{\mathrm{t}}}-\frac{1}{k_{yn}^{\mathrm{g}}+k_{ym}^{\mathrm{t}}}\right)\left\{\sin\left[k_{ym}^{\mathrm{t}}\left(\frac{b}{2}-\Delta y\right)\right]-(-1)^n\sin\left[k_{ym}^{\mathrm{t}}\left(\frac{b}{2}+\Delta y\right)\right]\right\};\quad (2)$$

$k_{ym}^{\mathrm{t}} = m\pi/b$ and $k_{yn}^{\mathrm{g}} = n\pi/(2\Delta y)$ are the y-directed DRWG wave numbers in the trough and gap subregions, respectively; k_{xm}^{t} and k_{xn}^{g} are the unknown x-directed DRWG wave numbers in the trough and gap subregions, respectively; and α_n and β_n are the unknown complex TE^z modal amplitudes. Note that $k_z = \sqrt{k_0^2-k_c^2} = \sqrt{k_0^2-\left(k_{ym}^{\mathrm{t}}\right)^2-\left(k_{xm}^{\mathrm{t}}\right)^2} = \sqrt{k_0^2-\left(k_{yn}^{\mathrm{g}}\right)^2-\left(k_{xn}^{\mathrm{g}}\right)^2}$, where $k_0 = \omega\sqrt{\varepsilon_0\mu_0}$ and ω is the radian frequency. Thus, at cutoff ($k_z = 0$), the above matrix equation is of the form

$$\mathbf{A}(k_c)\begin{pmatrix}\boldsymbol{\alpha}\\ \boldsymbol{\beta}\end{pmatrix}=\begin{pmatrix}A_{11}(k_c) & A_{12}(k_c)\\ A_{21}(k_c) & A_{22}(k_c)\end{pmatrix}\begin{pmatrix}\boldsymbol{\alpha}\\ \boldsymbol{\beta}\end{pmatrix}=\mathbf{0},\quad (3)$$

where A_{11}, A_{12}, A_{21}, and A_{22} are $N \times N$ submatrices with A_{12} and A_{21} being diagonal.

[12] The cutoff wave number k_c is found by forcing an eigenvalue of $\mathbf{A}(k_c)$ to equal zero via numerical root search; $\begin{pmatrix}\boldsymbol{\alpha} & \boldsymbol{\beta}\end{pmatrix}^{\mathrm{T}}$ is then the associated eigenvector of that zero eigenvalue. There are an infinite number of wave numbers which satisfy (3), each corresponding to a distinct TE^z DRWG mode. The k_c which corresponds to the first zero of (3) is the dominant DRWG mode cutoff wave number.

[13] After k_c and $\begin{pmatrix}\boldsymbol{\alpha} & \boldsymbol{\beta}\end{pmatrix}^{\mathrm{T}}$ have been found, the TE^z transverse DRWG field expressions are given by

$$\begin{aligned}
E_x^{\mathrm{g}} &= \sum_n e_{xn}^{\mathrm{g}}\left[\frac{\beta_n-\alpha_n}{\sin\left(k_{xn}^{\mathrm{g}}\Delta x\right)}\cos(k_{xn}^{\mathrm{g}}x)+\frac{\beta_n+\alpha_n}{\cos\left(k_{xn}^{\mathrm{g}}\Delta x\right)}\sin(k_{xn}^{\mathrm{g}}x)\right]\sin\left[k_{yn}^{g}(y-\Delta y)\right]\\
E_x^{\mathrm{g}} &= -\sum_n e_{yn}^{\mathrm{g}}\left[\frac{\beta_n-\alpha_n}{\sin\left(k_{xn}^{g}\Delta x\right)}\sin\left(k_{xn}^{g}x\right)-\frac{\beta+\alpha_n}{\cos\left(k_{xn}^{g}\Delta x\right)}\cos\left(k_{xn}^{g}x\right)\right]\cos\left[k_{yn}^{g}(y-\Delta y)\right]\\
\boldsymbol{e}_t^{\mathrm{g}} &= \hat{\mathbf{x}}E_x^{\mathrm{g}}+\hat{\mathbf{y}}E_y^{\mathrm{g}}\\
\boldsymbol{h}_t^{\mathrm{g}} &= \frac{\hat{\mathbf{z}}\times\boldsymbol{e}_t^{\mathrm{g}}}{Z^{\mathrm{TE}}}
\end{aligned}\quad (4)$$

in the $|x| < \Delta x$ (gap) subregion,

$$\begin{aligned}
E_x^{\mathrm{rt}} &= \sum_{n,m}\alpha_n e_{xn,m}^{\mathrm{t}}\cos\left[k_{xm}^{\mathrm{t}}\left(\frac{a}{2}-x\right)\right]\sin\left[k_{ym}^{\mathrm{t}}\left(y-\frac{b}{2}\right)\right]\\
E_y^{\mathrm{rt}} &= \sum_{n,m}\alpha_n e_{yn,m}^{\mathrm{t}}\sin\left[k_{xm}^{\mathrm{t}}\left(\frac{a}{2}-x\right)\right]\cos\left[k_{ym}^{\mathrm{t}}\left(y-\frac{b}{2}\right)\right]\\
\boldsymbol{e}_t^{\mathrm{rt}} &= \hat{\mathbf{x}}E_x^{\mathrm{rt}}+\hat{\mathbf{y}}E_y^{\mathrm{rt}}\\
\boldsymbol{h}_t^{\mathrm{rt}} &= \frac{\hat{\mathbf{z}}\times\boldsymbol{e}_t^{\mathrm{rt}}}{Z^{\mathrm{TE}}}
\end{aligned}\quad (5)$$

in the $x > \Delta x$ (right) trough subregion, and

$$\begin{aligned}
E_x^{\mathrm{lt}} &= -\sum_{n,m}\beta_n e_{xn,m}^{\mathrm{t}}\cos\left[k_{xm}^{\mathrm{t}}\left(\frac{a}{2}+x\right)\right]\sin\left[k_{ym}^{\mathrm{t}}\left(y-\frac{b}{2}\right)\right]\\
E_y^{\mathrm{lt}} &= \sum_{n,m}\beta_n e_{yn,m}^{\mathrm{t}}\sin\left[k_{xm}^{\mathrm{t}}\left(\frac{a}{2}+x\right)\right]\cos\left[k_{ym}^{\mathrm{t}}\left(y-\frac{b}{2}\right)\right]\\
\boldsymbol{e}_t^{\mathrm{lt}} &= \hat{\mathbf{x}}E_x^{\mathrm{lt}}+\hat{\mathbf{y}}E_y^{\mathrm{lt}}\\
\boldsymbol{h}_t^{\mathrm{lt}} &= \frac{\hat{\mathbf{z}}\times\boldsymbol{e}_t^{\mathrm{lt}}}{Z^{\mathrm{TE}}}
\end{aligned}\quad (6)$$

in the $x < -\Delta x$ (left) trough subregion. In the above field expressions, $Z^{\mathrm{TE}} = \omega\mu_0/k_z$ is the TE^z wave impedance and

$$\begin{aligned}
e_{xn}^{\mathrm{g}} &= \frac{k_{yn}^{\mathrm{g}}}{2k_{xn}^{\mathrm{g}}}\\
e_{yn}^{\mathrm{g}} &= \frac{1}{2}\\
e_{xn,m}^{\mathrm{t}} &= \frac{k_{ym}^{\mathrm{t}}\psi_{m,n}}{k_{xm}^{\mathrm{t}}\frac{b}{2}(1+\delta_{m0})\sin\left[k_{xm}^{\mathrm{t}}\left(\frac{a}{2}-\Delta x\right)\right]}\\
e_{yn,m}^{\mathrm{t}} &= \frac{\psi_{m,n}}{\frac{b}{2}(1+\delta_{m0})\sin\left[k_{xm}^{\mathrm{t}}\left(\frac{a}{2}-\Delta x\right)\right]}
\end{aligned}.\quad (7)$$

Note that modes which have even E_y and H_x distributions about the origin possess the relationship that $\alpha_n = \beta_n$ for $n = 0, 2, 4, \cdots$ and $\alpha_n = \beta_n = 0$ for $n = 1, 3, 5, \cdots$. This class of modes includes the DRWG dominant mode. A plot of the dominant DRWG mode is shown in Figure 2. The DRWG fields for $z < 0$ are

$$\begin{aligned}
\boldsymbol{E} &= \left(e^{-\mathrm{j}k_z z}+\Gamma e^{\mathrm{j}k_z z}\right)\begin{cases}\boldsymbol{e}_t^{\mathrm{g}}(\boldsymbol{\rho}) & |x|<\Delta x\\ \boldsymbol{e}_t^{\mathrm{lt}}(\boldsymbol{\rho}) & x<-\Delta x\\ \boldsymbol{e}_t^{\mathrm{rt}}(\boldsymbol{\rho}) & x>\Delta x\end{cases}\\
\boldsymbol{H} &= \left(e^{-\mathrm{j}k_z z}-\Gamma e^{\mathrm{j}k_z z}\right)\begin{cases}\boldsymbol{h}_t^{\mathrm{g}}(\boldsymbol{\rho}) & |x|<\Delta x\\ \boldsymbol{h}_t^{\mathrm{lt}}(\boldsymbol{\rho}) & x<-\Delta x\\ \boldsymbol{h}_t^{\mathrm{rt}}(\boldsymbol{\rho}) & x>\Delta x\end{cases}
\end{aligned}\quad (8)$$

and for $z > d$ are

$$\begin{aligned}
\boldsymbol{E} &= \mathrm{T}e^{-\mathrm{j}k_z(z-d)}\begin{cases}\boldsymbol{e}_t^{\mathrm{g}}(\boldsymbol{\rho}) & |x|<\Delta x\\ \boldsymbol{e}_t^{\mathrm{lt}}(\boldsymbol{\rho}) & x<-\Delta x\\ \boldsymbol{e}_t^{\mathrm{rt}}(\boldsymbol{\rho}) & x>\Delta x\end{cases}\\
\boldsymbol{H} &= \mathrm{T}e^{-\mathrm{j}k_z(z-d)}\begin{cases}\boldsymbol{h}_t^{\mathrm{g}}(\boldsymbol{\rho}) & |x|<\Delta x\\ \boldsymbol{h}_t^{\mathrm{lt}}(\boldsymbol{\rho}) & x<-\Delta x\\ \boldsymbol{h}_t^{\mathrm{rt}}(\boldsymbol{\rho}) & x>\Delta x\end{cases}
\end{aligned},\quad (9)$$

where $\Gamma = S_{11}^{\mathrm{thy}}$ and $\mathrm{T} = S_{21}^{\mathrm{thy}}$ are the desired theoretical reflection and transmission coefficients.

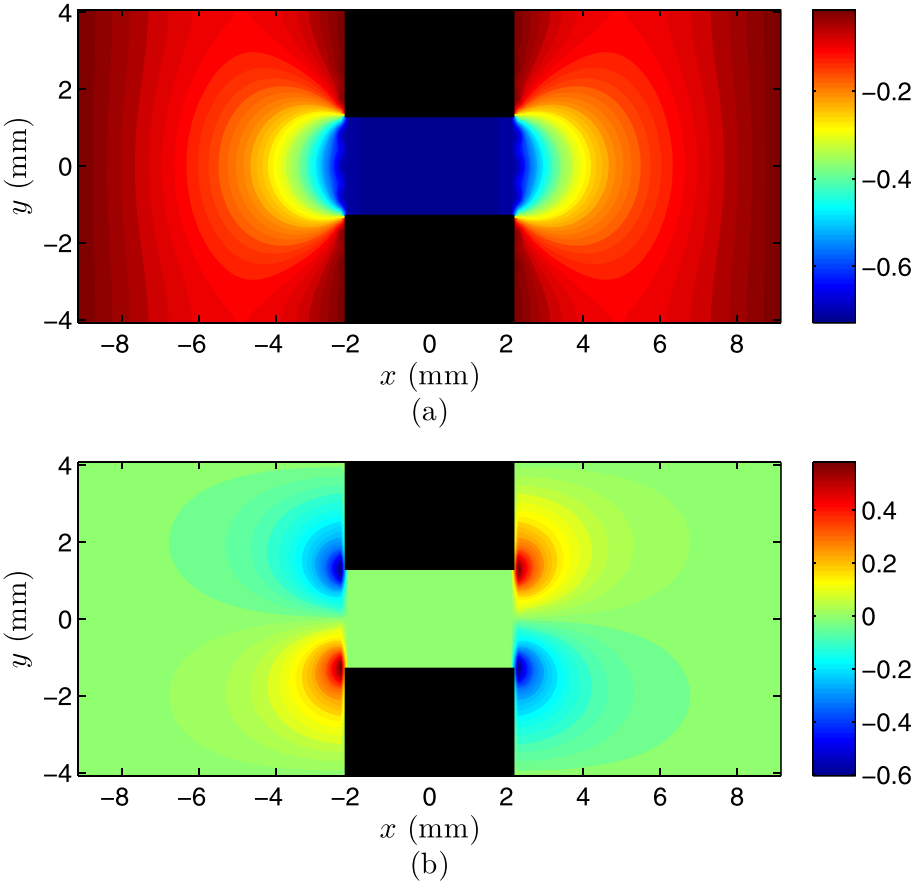

Figure 2. Dominant DRWG mode: (a) E_y field distribution and (b) E_x field distribution. This depiction of the dominant DRWG mode was generated using one gap mode and 20 trough modes.

2.2. Parallel-Plate Region Fields and Coupled MFIEs

[14] The transverse magnetic field in the parallel-plate region of the clamped DRWG structure is found by replacing the DRWG apertures with equivalent magnetic currents, $\mathcal{M}_1$ and $\mathcal{M}_2$, which emanate in the presence of the background structure [*Collin*, 1991; *Peterson et al.*, 1998]. The transverse magnetic field is given by

$$\boldsymbol{H}_t^{\mathrm{pp}}(\boldsymbol{\rho}, z) = \frac{1}{\mathrm{j}\omega\mu\varepsilon}(k^2 + \nabla_t\nabla\cdot)\boldsymbol{F}(\boldsymbol{\rho}, z), \tag{10}$$

where the electric vector potential $\boldsymbol{F}$ is

$$\boldsymbol{F}(\boldsymbol{\rho}, z) = \iint_S \mathbf{G}(\boldsymbol{\rho}, z|\,\boldsymbol{\rho}', 0)\cdot\varepsilon\mathcal{M}_1(\boldsymbol{\rho}')\mathrm{d}S' + \iint_S \mathbf{G}(\boldsymbol{\rho}, z|\,\boldsymbol{\rho}', d)\cdot\varepsilon\mathcal{M}_2(\boldsymbol{\rho}')\mathrm{d}S', \tag{11}$$

$\mathbf{G}$ is the dyadic magnetic-current-excited parallel-plate Green's function [*Hanson and Yakovlev*, 2001], $\boldsymbol{\rho} = \hat{\boldsymbol{x}}x + \hat{\boldsymbol{y}}y$ is the observation vector, $\boldsymbol{\rho}' = \hat{\boldsymbol{x}}x' + \hat{\boldsymbol{y}}y'$ is the source vector, and S represents the DRWG aperture cross sections.

[15] Based upon the expressions for the transverse fields in the DRWG and parallel-plate regions of the structure in Figure 1, a system of coupled MFIEs can be derived by enforcing the continuity of the transverse magnetic fields at $z = 0$ and $z = d$:

$$\frac{1}{\mathrm{j}\omega\mu\varepsilon}(k^2 + \nabla_t\nabla\cdot)\boldsymbol{F}(\boldsymbol{\rho}, 0) = (1 - \Gamma)\begin{cases}\boldsymbol{h}_t^{\mathrm{g}}(\boldsymbol{\rho}) & |x| < \Delta x \\ \boldsymbol{h}_t^{\mathrm{lt}}(\boldsymbol{\rho}) & x < -\Delta x \\ \boldsymbol{h}_t^{\mathrm{rt}}(\boldsymbol{\rho}) & x > \Delta x\end{cases} \quad \boldsymbol{\rho} \in S$$
$$\frac{1}{\mathrm{j}\omega\mu\varepsilon}(k^2 + \nabla_t\nabla\cdot)\boldsymbol{F}(\boldsymbol{\rho}, d) = \mathrm{T}\begin{cases}\boldsymbol{h}_t^{\mathrm{g}}(\boldsymbol{\rho}) & |x| < \Delta x \\ \boldsymbol{h}_t^{\mathrm{lt}}(\boldsymbol{\rho}) & x < -\Delta x \\ \boldsymbol{h}_t^{\mathrm{rt}}(\boldsymbol{\rho}) & x > \Delta x\end{cases} \quad \boldsymbol{\rho} \in S \tag{12}$$

where $k = \omega\sqrt{\varepsilon\mu}$ and ε and μ are the permittivity and permeability of the material filling the parallel-plate region (i.e., the MUT). The unknowns in the above MFIEs are $\mathcal{M}_1$, $\mathcal{M}_2$, Γ, and T.

2.3. MoM Solution and Computation of Impedance Matrix Elements

[16] Solving (12) for Γ and T is accomplished using the MoM [*Harrington*, 1993; *Peterson et al.*, 1998]. The first step in the MoM is to choose suitable basis functions to represent the unknown currents, $\mathcal{M}_1$ and $\mathcal{M}_2$. Since $\mathcal{M}_1$ and $\mathcal{M}_2$ are related to the transverse DRWG aperture electric fields, it makes physical and mathematical sense to expand

$\boldsymbol{\mathcal{M}}_1$ and $\boldsymbol{\mathcal{M}}_2$ using the electric field distributions given in (4)–(6), namely,

$$\begin{aligned}\boldsymbol{\mathcal{M}}_1(\boldsymbol{\rho}') &= -\hat{\boldsymbol{n}} \times \boldsymbol{E} = -\hat{\boldsymbol{z}} \times (1+\Gamma) \begin{cases} \boldsymbol{e}_t^{\mathrm{g}}(\boldsymbol{\rho}') & |x| < \Delta x \\ \boldsymbol{e}_t^{\mathrm{lt}}(\boldsymbol{\rho}') & x < -\Delta x \\ \boldsymbol{e}_t^{\mathrm{rt}}(\boldsymbol{\rho}') & x > \Delta x \end{cases} \\ \boldsymbol{\mathcal{M}}_2(\boldsymbol{\rho}') &= -\hat{\boldsymbol{n}} \times \boldsymbol{E} = \hat{\boldsymbol{z}} \times \mathrm{T} \begin{cases} \boldsymbol{e}_t^{\mathrm{g}}(\boldsymbol{\rho}') & |x| < \Delta x \\ \boldsymbol{e}_t^{\mathrm{lt}}(\boldsymbol{\rho}') & x < -\Delta x \\ \boldsymbol{e}_t^{\mathrm{rt}}(\boldsymbol{\rho}') & x > \Delta x \end{cases} \end{aligned}, \tag{13}$$

where $\hat{\boldsymbol{n}}$, the unit normal vector, points into the MUT region. Substitution of (13) into (12) and subsequent testing (the final step in the MoM) using the transverse magnetic field distributions given in (4)–(6) yields a 2×2 matrix equation:

$$\mathbf{A} \begin{pmatrix} \Gamma \\ \mathrm{T} \end{pmatrix} = \begin{pmatrix} a_{11} & a_{12} \\ a_{21} & a_{22} \end{pmatrix} \begin{pmatrix} \Gamma \\ \mathrm{T} \end{pmatrix} = \boldsymbol{b}, \tag{14}$$

where $\mathbf{A}$ is the impedance matrix and $\boldsymbol{b}$ is a vector containing the incident field excitation. Impedance matrix elements a_{11} and a_{22} are the "self" terms. They model how a source located at port 1 affects an observer located at port 1 and vice versa. Elements a_{12} and a_{21} are the "coupling" terms. They model how a source at port 1 affects an observer at port 2 and vice versa. Note that $a_{11} = a_{22}$ because of the symmetry of the clamped DRWG probe and $a_{12} = a_{21}$ because of reciprocity.

[17] Computing the elements of $\mathbf{A}$ can be accomplished by directly computing the convolution integrals in (11). This approach requires the numerical evaluation of four integrals (two basis and two testing integrals) for each integral in (11). It is numerically advantageous to apply the convolution theorem and perform the required integrations in the spectral domain [*Hyde et al.*, 2012]. This approach permits all the basis and testing integrals to be computed in closed form yielding spectral domain integrals which, in the worst computational cases, are given by

$$\sum_{n,m} \sum_{\tilde{n},\tilde{m}} e^{\mathrm{t}}_{yn,m} e^{\mathrm{t}}_{y\tilde{n},\tilde{m}} \int_{-\infty}^{\infty} (k^2 - \xi^2) f_{m,\tilde{m}}(\xi) \int_{-\infty}^{\infty} \frac{\cosh(pd)}{p \sinh(pd)} g_{m,\tilde{m}}(\eta) \mathrm{d}\eta \mathrm{d}\xi, \tag{15}$$

where $p = \sqrt{\xi^2 + \eta^2 - k^2}$ is the spectral domain wave number and

$$\begin{aligned} f_{m,\tilde{m}}(\xi) &= \int_{\Delta x}^{a/2} \sin\left[k^{\mathrm{t}}_{xm}\left(\frac{a}{2} - x'\right)\right] \cos(\xi x') \mathrm{d}x' \\ &\quad \cdot \int_{\Delta x}^{a/2} \sin\left[k^{\mathrm{t}}_{x\tilde{m}}\left(\frac{a}{2} - x\right)\right] \cos(\xi x) \mathrm{d}x \\ g_{m,\tilde{m}}(\eta) &= \int_{-b/2}^{b/2} \cos\left[k^{\mathrm{t}}_{ym}\left(y' - \frac{b}{2}\right)\right] e^{-\mathrm{j}\eta y'} \mathrm{d}y' \\ &\quad \cdot \int_{-b/2}^{b/2} \cos\left[k^{\mathrm{t}}_{y\tilde{m}}\left(y - \frac{b}{2}\right)\right] e^{\mathrm{j}\eta y} \mathrm{d}y \end{aligned} \tag{16}$$

[18] The η integral can be evaluated using complex-plane analysis yielding a pole-series representation. The remaining ξ integral contains irremovable branch cuts and is therefore most easily computed numerically [*Hyde and Havrilla*, 2008; *Hyde et al.*, 2009b; *Stewart and Havrilla*, 2006]. It should be noted that due to the summations in the basis and testing functions, special care must be taken when computing the spectral domain integrals. For optimal computational efficiency, it is best to bring the summations inside the ξ integral, evaluate the η integral via complex-plane analysis, evaluate the resulting summations, and lastly, calculate the ξ integral numerically. Note that there are a total of 32 distinct spectral domain integrals which must be evaluated.

[19] It should be stated that one could use a commercial EM solver to perform the theoretical work presented here. However, to yield theoretical *S*-parameters of sufficient accuracy to obtain accurate ε_r and μ_r values would require a very high-density mesh of the measurement structure, especially in the vicinity of the DRWG apertures and the parallel-plate/MUT region. This would significantly affect the computation time. The fact that iteration is required to find ε_r and μ_r only makes computation time more prohibitive. On the other hand, the method of analysis utilized here, being based on the equivalence theorem, only requires discretization of the unknown aperture surface currents. This produces a significant reduction in the size of the problem and computational burden when compared to finite element and finite difference time domain solvers. Also, by utilizing the approach presented here, significant physical insight into the field behavior in the structure is gained. One of the drawbacks of the proposed approach is that the effects of higher-order DRWG modes generated at the DRWG apertures are not included. These effects are included in commercial solvers. Future research will include the effects of higher-order DRWG modes in this technique.

3. Experimental Validation

[20] In this section, the technique introduced above is experimentally validated. Before progressing to the analysis of the experimental results, discussions of the experimental apparatus and procedure are warranted.

3.1. System Description and Measurement Procedure

[21] In this experiment, material characterization measurements were made at 6–18 GHz (as opposed to 8–12 GHz for traditional X-band rectangular waveguide probes) of two lossy silicon-based magnetic absorbing materials, ECCOSORB® FGM-125 (d = 3.12 mm) and ECCOSORB® SF-3 (d = 1.85 mm) manufactured by *Emerson & Cuming Microwave Products* [2012, 2007], using an Agilent E8362B vector network analyzer [*Agilent Technologies*, 2008]. The clamped DRWG apparatus consisted of two WRD650 DRWGs (a = 18.29 mm, b = 8.15 mm, Δx = 2.20 mm, and Δy = 1.28 mm) connected via screws to two aluminum flange plates. On the side of the flange plates which were connected to the DRWGs, 3.18 mm alignment holes were machined to ensure precision alignment between the DRWG and the flange-plate apertures. To ensure good alignment of the port 1 and port 2 apertures, i.e., the flange-plate apertures in contact with the MUT, 3.18 mm alignment holes were also machined on the outer edges of the flange plates. Locking pliers were used in the areas around the DRWG/flange-plate apertures to ensure good contact between the flange plates and the MUT. A photograph of the apparatus is shown in Figure 3. Note

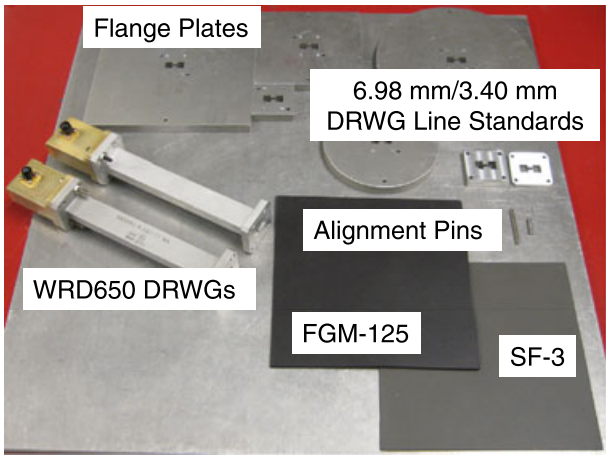

Figure 3. Photograph of the clamped DRWG apparatus with parts labeled.

that square and circular aluminum flange plates of several different dimensions were machined: 15.24 cm × 15.24 cm × 0.95 cm, 10.16 cm × 10.16 cm × 0.95 cm, and 3.81 cm × 3.81 cm × 0.95 cm (square) and 15.24 cm diameter × 0.95 cm and 10.16 cm diameter × 0.95 cm (circular).

[22] Before the material measurements were made, the apparatus was calibrated using a thru-reflect-line (TRL) calibration [*Engen and Hoer*, 1979]. Two custom-made DRWG line standards were used in the calibration—one 6.98 mm thick to cover 6–12 GHz and one 3.40 mm thick to cover 12–18 GHz. These line standards can be seen in the photograph in Figure 3. The TRL calibration placed the port 1 and port 2 calibration planes at the DRWG apertures. These calibration planes were then phase shifted to their desired locations, i.e., the front (desired port 1 calibration plane location) and back (desired port 2 calibration plane location) faces of the MUT, by

$$S_{mn}^{\text{meas}} = S_{mn}^{\text{TRL}} \exp(2\mathrm{j}k_z h), \tag{17}$$

where $m, n = 1, 2$ and $h = 0.95$ cm is the flange-plate thickness.

[23] The ε_r and μ_r of the MUTs were found by minimizing the root-mean-square difference between the theoretical $\boldsymbol{S}^{\text{thy}}$ and measured $\boldsymbol{S}^{\text{meas}}$ S-parameters using Broyden's method [*Broyden*, 1965], namely,

$$\begin{pmatrix} \hat{\varepsilon}_r \\ \hat{\mu}_r \end{pmatrix} = \underset{\varepsilon_r, \mu_r \in \mathbb{C}}{\arg\min} \left\| \boldsymbol{S}^{\text{thy}}(f; \varepsilon_r, \mu_r) - \boldsymbol{S}^{\text{meas}}(f) \right\|_2, \tag{18}$$

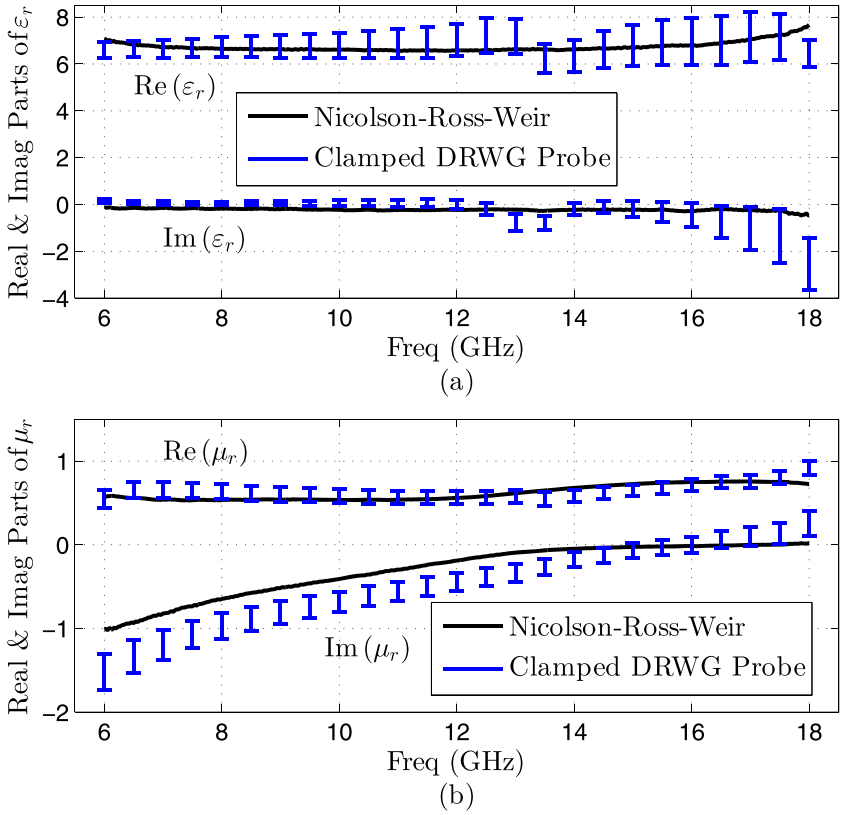

Figure 4. ECCOSORB® FGM-125 material characterization results. (a) Relative complex permittivity of FGM-125 using the clamped DRWG probe (blue bars) and the traditional Nicolson-Ross-Weir technique (solid black traces). (b) Relative complex permeability of FGM-125 using the clamped DRWG probe (blue bars) and the traditional Nicolson-Ross-Weir technique (solid black traces). The widths of the bars in the plots represent the errors in the ε_r and μ_r measurements ($\pm 2\Delta\varepsilon_r$ and $\pm 2\Delta\mu_r$, respectively) considering the S-parameter measurement uncertainties specified in the vector network analyzer data sheet and ± 0.1 mm measurement uncertainties in d and h.

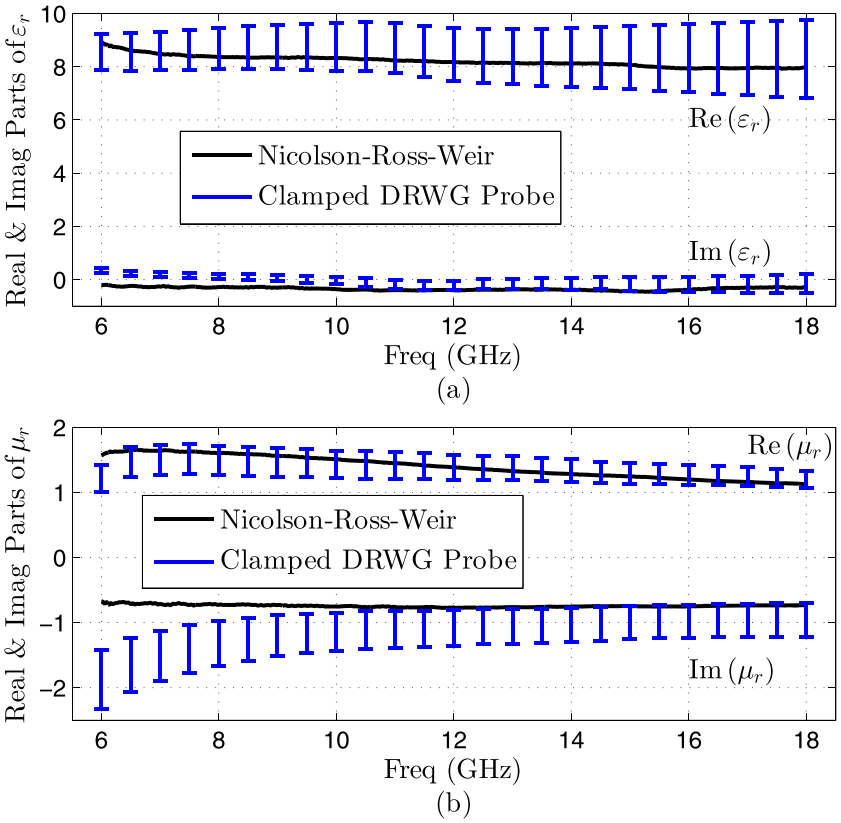

Figure 5. ECCOSORB® SF-3 material characterization results. (a) Relative complex permittivity of SF-3 using the clamped DRWG probe (blue bars) and the traditional Nicolson-Ross-Weir technique (solid black traces). (b) Relative complex permeability of SF-3 using the clamped DRWG probe (blue bars) and the traditional Nicolson-Ross-Weir technique (solid black traces). The widths of the bars in the plots represent the errors in the ε_r and μ_r measurements ($\pm 2\Delta\varepsilon_r$ and $\pm 2\Delta\mu_r$, respectively) considering the *S*-parameter measurement uncertainties specified in the vector network analyzer data sheet and ± 0.1 mm measurement uncertainties in d and h.

where $\boldsymbol{S} = \left(S_{11}\ S_{21}\ S_{12}\ S_{22}\right)^{\mathrm{T}}$ and f is the frequency. Note that $S_{11}^{\mathrm{thy}} = S_{22}^{\mathrm{thy}}$ and $S_{21}^{\mathrm{thy}} = S_{12}^{\mathrm{thy}}$ because of measurement geometry symmetry and electromagnetic reciprocity, respectively.

3.2. Experimental Results

[24] Figures 4 and 5 show the relative ε_r (Figures 4a and 5a) and μ_r (Figures 4b and 5b) results for ECCOSORB® FGM-125 and ECCOSORB® SF-3, respectively. The clamped DRWG results are demarcated by the blue bars. The destructive Nicolson-Ross-Weir results, provided to serve as a reference, are demarcated by the solid black traces. Note that the Nicolson-Ross-Weir results were obtained by measuring FGM-125 and SF-3 samples which were carefully machined to uniformly fill the WRD650 DRWG aperture. Ensuring the samples uniformly fill the DRWG aperture is very difficult and paramount because the presence of air gaps, especially in the vicinity of the DRWG gap subregion where the dominant-mode fields are the strongest (see Figure 2), can cause very large variations in the extracted ε_r and μ_r values. To the authors' knowledge, this is the first time that DRWGs have been used to characterize materials via the Nicolson-Ross-Weir technique.

[25] The widths of the bars in the figures represent the errors in the clamped DRWG probe ε_r and μ_r measurements ($\pm 2\Delta\varepsilon_r$ and $\pm 2\Delta\mu_r$, respectively) considering the *S*-parameter measurement uncertainties $\left(\Delta S_{mn}^{\mathrm{meas}}\right)$ specified in the vector network analyzer data sheet [*Agilent Technologies*, 2008] and ± 0.1 mm measurement uncertainties in d and h (Δd and Δh) [*Baker-Jarvis et al.*, 1990]:

$$\begin{aligned}\left(\Delta\varepsilon_r^{\mathrm{r}}\right)^2 = &\sum_{m=1}^{2}\sum_{n=1}^{2}\left(\frac{\partial\varepsilon_r^{\mathrm{r}}}{\partial S_{mn}^{\mathrm{meas,\,r}}}\Delta S_{mn}^{\mathrm{meas,\,r}}\right)^2 \\ &+\sum_{m=1}^{2}\sum_{n=1}^{2}\left(\frac{\partial\varepsilon_r^{\mathrm{r}}}{\partial S_{mn}^{\mathrm{meas,\,i}}}\Delta S_{mn}^{\mathrm{meas,\,i}}\right)^2, \\ &+\left(\frac{\partial\varepsilon_r^{\mathrm{r}}}{\partial d}\Delta d\right)^2+\left(\frac{\partial\varepsilon_r^{\mathrm{r}}}{\partial h}\Delta h\right)^2\end{aligned} \tag{19}$$

where the superscripts "r" and "i" denote the real and imaginary parts, respectively. The values for $\Delta\varepsilon_r^{\mathrm{i}}$, $\Delta\mu_r^{\mathrm{r}}$, and $\Delta\mu_r^{\mathrm{i}}$ are calculated in a similar manner as above. Note that the partial derivatives in (19) were calculated numerically using the forward difference approximation. The ε_r and μ_r errors calculated using (19) are worst case estimates [*Baker-Jarvis et al.*, 1990]. Because some of the bar widths in the figures

Table 1. Mean, Maximum, and Minimum of $\Delta\varepsilon_r$ and $\Delta\mu_r$ for FGM-125 and SF-3

FGM-125			
	Mean	Max	Min
$\Delta\varepsilon_r^{\mathrm{r}}$	0.3301	0.5407	0.1638
$\Delta\varepsilon_r^{\mathrm{i}}$	0.1608	0.5762	0.0356
$\Delta\mu_r^{\mathrm{r}}$	0.0411	0.0527	0.0351
$\Delta\mu_r^{\mathrm{i}}$	0.0630	0.1100	0.0446
SF-3			
	Mean	Max	Min
$\Delta\varepsilon_r^{\mathrm{r}}$	0.5118	0.7390	0.3457
$\Delta\varepsilon_r^{\mathrm{i}}$	0.0967	0.1852	0.0382
$\Delta\mu_r^{\mathrm{r}}$	0.0940	0.1140	0.0673
$\Delta\mu_r^{\mathrm{i}}$	0.1490	0.2276	0.1268

are hard to discern, a summary of the $\Delta\varepsilon_r$ and $\Delta\mu_r$ values obtained for FGM-125 and SF-3 is provided in Table 1.

[26] Overall, there is fairly good agreement between the clamped DRWG probe and reference Nicolson-Ross-Weir traces. The main discrepancy between the two occurs in the results for magnetic loss with the clamped DRWG probe generally over-predicting the amount of loss. This over-prediction of magnetic loss has precedent in the literature for similar probe geometries [*Hyde et al.*, 2011; *Hyde and Havrilla*, 2008; *Hyde et al.*, 2009b]. In all cases cited, the problem is alleviated when higher-order modes are included in the analytical model (recall that only the dominant DRWG mode is considered here). While including higher-order modes in rectangular waveguide probe systems is a relatively straightforward process and has been accomplished by many researchers [*Stewart and Havrilla*, 2006; *Bois et al.*, 1999; *Chang et al.*, 1997; *Hyde and Havrilla*, 2008; *Hyde et al.*, 2009b; *Maode et al.*, 1998; *Seal et al.*, 2012; *Hyde et al.*, 2012], because of the complexity of DRWG fields, including higher-order modes in the clamped DRWG probe analysis is a very difficult theoretical and computational problem. Including higher-order modes in the clamped DRWG probe is left to future work. Note that other lossy materials were measured as part of this analysis, in particular, resistive cards (R-cards) [*Hyde et al.*, 2009a; *Costa*, 2013; *Glover et al.*, 2008; *Massman et al.*, 2010]. The results were similar to those just presented and therefore are not shown here for the sake of brevity.

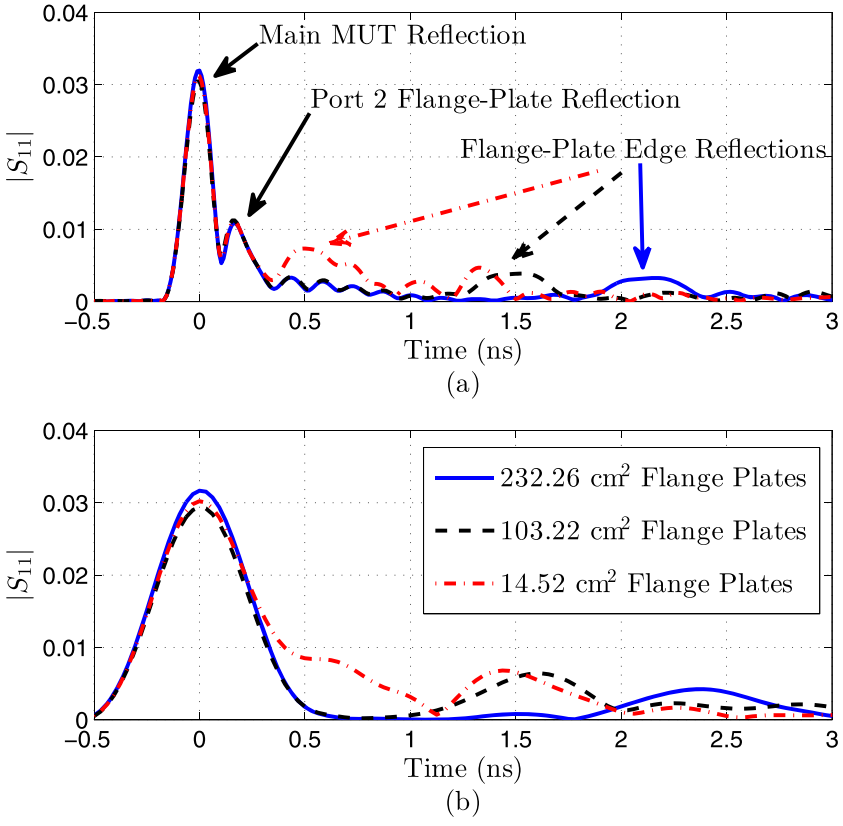

Figure 6. $|S_{11}|$ time-domain plots of a 6.43 mm thick sample of 99.5% Al_2O_3 ($\varepsilon_r \approx 9 - j0$, $\mu_r \approx 1 - j0$) using 15.24 cm × 15.24 cm (solid blue traces), 10.16 cm × 10.16 cm (dashed black traces), and 3.81 cm × 3.81 cm (dash-dotted red traces) square flange plates. (a) Time-domain $|S_{11}|$ traces using the full 12 GHz WRD650 DRWG measurement bandwidth. (b) Time-domain $|S_{11}|$ traces using a 4 GHz measurement bandwidth, i.e., representative of X-band rectangular waveguide probe systems. The flange-plate edge reflections, port 2 flange-plate reflection, and the main MUT reflection are clearly resolved for all flange-plate sizes using the full DRWG bandwidth. Using the representative X-band rectangular waveguide bandwidth, only the main MUT reflection and the flange-plate edge reflections using the 15.24 cm × 15.24 cm and 10.16 cm × 10.16 cm are resolved.

3.3. Discussion on Characterizing Low-Loss MUTs

[27] While the presented experimental results focused on the characterization of lossy materials, the clamped DRWG apparatus can also be used to characterize low-loss MUTs. Characterization results of low-loss MUTs are not presented here for the sake of brevity; however, a brief discussion of the measurement procedure follows.

[28] For low-loss MUTs as opposed to lossy MUTs, reflections from the flange-plate edges can corrupt the measured *S*-parameters. These reflections must either be accounted for analytically (a very difficult problem) or removed from the measured *S*-parameters via time-domain gating [*Hyde et al.*, 2011] to effectively model flange plates of infinite dimensions.

[29] To use the latter technique, the characterization measurement must possess sufficient bandwidth to resolve the flange-plate edge reflections. The criterion is

$$B = \frac{c}{2\rho\sqrt{\varepsilon_r \mu_r}}, \tag{20}$$

where B is the minimum required measurement bandwidth, $c/\sqrt{\varepsilon_r \mu_r}$ is the speed of light in the MUT, and ρ is the radius of the flange plate [*Hyde et al.*, 2011]. Since in most characterization experiments the measurement bandwidth is known a priori, it is more useful to solve (20) for ρ. In this context, ρ represents the minimum flange-plate radius in which the edge reflections will be resolvable and thus removable via time-domain gating. In other words, ρ is the probe's measurement footprint [*Hyde et al.*, 2011]. Note that special care must be taken when using this relation. Common signal processing techniques, like frequency-domain windowing used to suppress side lobes in the time-domain response, will affect the resolution. It should also be mentioned that time-domain gating can introduce unwanted effects at the measurement frequency band edges thereby reducing the "usable" measurement bandwidth [*Hyde et al.*, 2011]. For the DRWGs used in the research, the usable measurement bandwidth after time-domain gating will be reduced by 2–4 GHz.

[30] Nevertheless, the much broader bandwidth of the clamped DRWG probe compared to other waveguide probes means that much smaller flange plates (sizes $\propto 1/B$) can be used to characterize materials. This is demonstrated in Figure 6. The figure shows measured time-domain $|S_{11}|$ plots of a 6.43 mm thick sample of 99.5% Al_2O_3 ($\varepsilon_r \approx 9$–j0, $\mu_r \approx 1$ – j0) using 15.24 cm × 15.24 cm (solid blue traces), 10.16 cm × 10.16 cm (dashed black traces), and 3.81 cm × 3.81 cm (dash-dotted red traces) square flange plates. Note that the S_{11} frequency-domain data were windowed using a Kaiser window ($\beta = 6$) prior to Fourier transforming to arrive at the plotted time-domain responses [*Oppenheim and Schafer*, 2010]. Figure 6a shows the time-domain $|S_{11}|$ traces when the full 12 GHz WRD650 DRWG measurement bandwidth is used; Figure 6b shows the same traces when a 4 GHz bandwidth (representative of X-band rectangular waveguide probe systems) is used.

[31] It is clear from the results presented in the figure that the bandwidth of the clamped DRWG probe is sufficient to resolve the flange-plate edge reflections (labeled on the figure) for all three flange-plate sizes, while an X-band rectangular waveguide probe is only able to resolve the edge reflections for the 15.24 cm × 15.24 cm and 10.16 cm × 10.16 cm flange plates. Indeed, the bandwidth of the clamped DRWG probe is large enough to resolve the reflection from the port 2 flange plate, located on the backside of the MUT approximately 6.43 mm from the port 1 DRWG aperture. The additional bandwidth inherent in the clamped DRWG probe allows for the use of small flange plates making it especially attractive for nondestructive inspection/evaluation applications in the field or for the nondestructive characterization of small specimens.

4. Conclusion

[32] In this paper, a novel two-port probe system was presented which used DRWGs to provide nondestructive, broadband characterization of planar MUTs. The probe possessed approximately 2 to 3 times the bandwidth of traditional coaxial and rectangular/circular waveguide probe systems in the literature while maintaining the structural robustness characteristic of rectangular/circular waveguide probe systems. The theoretical development of the probe was discussed in section 2. Theoretical expressions for the reflection and transmission coefficients, necessary for extracting ε_r and μ_r of the MUT via numerical inversion, were derived by applying Love's equivalence theorem, enforcing transverse field continuity at the DRWG apertures, and solving the resulting coupled MFIEs via the MoM. Section 3 presented experimental characterization results of two magnetic absorbing materials using the new two-port probe. The probe's errors in determining ε_r and μ_r considering measured *S*-parameter, MUT thickness, and flange-plate thickness uncertainties were also examined. It was found that the results using the probe compared well with the destructive, traditional Nicolson-Ross-Weir results with the exception of magnetic loss; this discrepancy is due to considering only the dominant DRWG mode in the presented analysis. Last, measured reflection coefficient time-domain data of a low-loss material were analyzed. It was shown and discussed how the much larger bandwidth inherent with the new DRWG probe allows for the use of smaller flange plates making it an especially attractive option for nondestructive inspection/evaluation applications in the field or for the nondestructive characterization of small specimens.

[33] **Acknowledgments.** The views expressed in this paper are those of the authors and do not reflect the official policy or position of the U.S. Air Force, the Department of Defense, or the U.S. Government.

References

Agilent Technologies, Inc. (2008), *Technical Specifications Agilent Technologies PNA Series Network Analyzers E8362B/C, E8363B/C, and E8364B/C*, Santa Clara, Calif.

Baker-Jarvis, J., and M. D. Janezic (1996), Analysis of a two-port flanged coaxial holder for shielding effectiveness and dielectric measurements of thin films and thin materials, *IEEE Trans. Electromagn. Compat.*, *38*(1), 67–70, doi:10.1109/15.485697.

Baker-Jarvis, J., E. Vanzura, and W. Kissick (1990), Improved technique for determining complex permittivity with the transmission/reflection method, *IEEE Trans. Microwave Theory Tech.*, *38*(8), 1096–1103, doi:10.1109/22.57336.

Baker-Jarvis, J., M. D. Janezic, P. D. Domich, and R. G. Geyer (1994), Analysis of an open-ended coaxial probe with lift-off for nondestructive testing, *IEEE Trans. Instrum. Meas.*, *43*(5), 711–718, doi:10.1109/19.328897.

Bird, T. (2004), Mutual coupling in arrays of coaxial waveguides and horns, *IEEE Trans. Antennas Propag.*, *52*, 821–829, doi:10.1109/TAP.2004.825487.

Bois, K. J., A. Benally, and R. Zoughi (1999), Multimode solution for the reflection properties of an open-ended rectangular waveguide radiating into a dielectric half-space: The forward and inverse problems, *IEEE Trans. Instrum. Meas.*, *48*(6), 1131–1140, doi:10.1109/19.816127.

Boybay, M. S., and O. M. Ramahi (2011), Open-ended coaxial line probes with negative permittivity materials, *IEEE Trans. Antennas Propag.*, *59*, 1765–1769, doi:10.1109/TAP.2011.2123056.

Broyden, C. G. (1965), A class of methods for solving nonlinear simultaneous equations, *Math. Comput.*, *19*, 577–593, doi:10.1090/S0025-5718-1965-0198670-6.

Chang, C.-W., K.-M. Chen, and J. Qian (1997), Nondestructive determination of electromagnetic parameters of dielectric materials at X-band frequencies using a waveguide probe system, *IEEE T. Instrum. Meas.*, *46*(5), 1084–1092, doi:10.1109/19.676717.

Chen, C.-P., Z. Ma, T. Anada, and J.-P. Hsu (2005), Further study on two-thickness-method for simultaneous measurement of complex EM parameters based on open-ended coaxial probe, *Paper presented at European Microwave Conference*, IEEE, Paris, doi:10.1109/EUMC.2005.1608904.

Cho, Y. H., and H. J. Eom (2001), Fourier transform analysis of a ridge waveguide and a rectangular coaxial line, *Radio Sci.*, *36*(4), 533–538, doi:10.1029/2000RS002381.

Collin, R. E. (1991), *Field Theory of Guided Waves,* 2nd ed., IEEE Press, New York.

Costa, F. (2013), Surface impedance measurement of resistive coatings at microwave frequencies, *IEEE Trans. Instrum. Meas.*, *62*(2), 432–437, doi:10.1109/TIM.2012.2217661.

De Langhe, P., K. Blomme, L. Martens, and D. De Zutter (1993), Measurement of low-permittivity materials based on a spectral-domain analysis for the open-ended coaxial probe, *IEEE Trans. Instrum. Meas.*, *42*(5), 879–886, doi:10.1109/19.252521.

De Langhe, P., L. Martens, and D. De Zutter (1994), Design rules for an experimental setup using an open-ended coaxial probe based on theoretical modelling, *IEEE Trans. Instrum. Meas.*, *43*(6), 810–817, doi:10.1109/19.368062.

Dester, G. D., E. J. Rothwell, M. J. Havrilla, and M. W. Hyde (2010), Error analysis of a two-layer method for the electromagnetic characterization of conductor-backed absorbing material using an open-ended waveguide probe, *PIER B*, *26*, 1–21, doi:10.2528/PIERB1008050.

Dester, G. D., E. J. Rothwell, and M. J. Havrilla (2012), Two-iris method for the electromagnetic characterization of conductor-backed absorbing materials using an open-ended waveguide probe, *IEEE Trans. Instrum. Meas.*, *61*, 1037–1044, doi:10.1109/TIM.2011.2174111.

Elliot, R. S. (1993), *An Introduction to Guided Waves and Microwave Circuits*, Prentice-Hall, Englewood Cliffs, N. J.

Emerson & Cuming Microwave Products, Inc. (2007), ECCOSORB® SF Thin, Flexible, Resonant Absorbers, Randolph, Mass.

Emerson & Cuming Microwave Products, Inc. (2012), ECCOSORB® FGM Thin, Flexible, Impervious, Broadband Absorbers, Randolph, Mass.

Engen, G. F., and C. A. Hoer (1979), Thru-reflect-line: An improved technique for calibrating the dual six-port automatic network analyzer, *IEEE Trans. Microwave Theory Tech.*, *27*(12), 987–993, doi:10.1109/TMTT.1979.1129778.

Folgerø, K., and T. Tjomsland (1996), Permittivity measurement of thin liquid layers using open-ended coaxial probes, *Meas. Sci. Technol.*, *7*(8), 1164–1173, doi:10.1088/0957-0233/7/8/012.

Ganchev, S. I., S. Bakhtiari, and R. Zoughi (1992), A novel numerical technique for dielectric measurement of generally lossy dielectrics, *IEEE Trans. Instrum. Meas.*, *41*(3), 361–365, doi:10.1109/19.153329.

Glover, B. B., K. W. Whites, M. W. Hyde, and M. J. Havrilla (2008), Complex effective permittivity of carbon loaded dielectric films with printed metallic square rings, *Proc 2nd Intern'l Cong. Ad. Electromagnet. Mat. Microw. Optics*, 762–764, International Congress on Advanced Electromagnetic Materials in Microwaves and Optics Virtual Institute for Artificial Electromagnetic Materials and Metamaterials "Metamorphose VI AISB" Pamplona, Spain.

Hanson, G. W., and A. B. Yakovlev (2001), *Operator Theory for Electromagnetics: An Introduction*, Springer, New York.

Harrington, R. (1993), *Field Computation by Moment Methods*, IEEE Press, New York.

Helszajn, J. (2000), *Ridge Waveguide and Passive Microwave Components*, Inst. of Electr. Eng., London.

Hopfer, S. (1955), The design of ridged waveguides, *IEEE Trans. Microwave Theory Tech.*, *3*(5), 20–29, doi:10.1109/TMTT.1955.1124972.

Hyde, M., M. Havrilla, and P. Crittenden (2009a), A novel method for determining the R-card sheet impedance using the transmission coefficient measured in free-space or waveguide systems, *IEEE Trans. Instrum. Meas.*, *58*(7), 2228–2233, doi:10.1109/TIM.2009.2013673.

Hyde, M., M. Havrilla, A. Bogle, E. Rothwell, and G. Dester (2012), An improved two-layer method for nondestructively characterizing magnetic sheet materials using a single rectangular waveguide probe, *Electromagnetics*, *32*, 411–425, doi:10.1080/027263432012.716702.

Hyde, M. W., and M. J. Havrilla (2008), A nondestructive technique for determining complex permittivity and permeability of magnetic sheet materials using two flanged rectangular waveguides, *PIER*, *79*, 367–386, doi:10.2528/PIER07102405.

Hyde, M. W., J. W. Stewart, M. J. Havrilla, W. P. Baker, E. J. Rothwell, and D. P. Nyquist (2009b), Nondestructive electromagnetic material characterization using a dual waveguide probe: A full wave solution, *Radio Sci.*, *44*, doi:10.1029/2008RS003937.

Hyde, M. W., M. J. Havrilla, and A. E. Bogle (2011), A novel and simple technique for measuring low-loss materials using the two flanged waveguides measurement geometry, *Meas. Sci. Technol.*, *22*(085704), doi:10.1088/0957-0233/22/8/085704.

Li, C.-L., and K.-M. Chen (1995), Determination of electromagnetic properties of materials using flanged open-ended coaxial probe—Full-wave analysis, *IEEE Trans. Instrum. Meas.*, *44*(1), 19–27, doi:10.1109/19.368108.

Maode, N., S. Yong, Y. Jinkui, F. Chenpeng, and X. Deming (1998), An improved open-ended waveguide measurement technique on parameters ε_r and μ_r of high-loss materials, *IEEE Trans. Instrum. Meas.*, *47*(2), 476–481, doi:10.1109/19.744194.

Massman, J., M. Havrilla, K. Whites, and M. Hyde (2010), A stepped flange waveguide technique for determining tapered R-card sheet impedance, *Paper presented at Asia-Pacific Microwave Conference*, 1769–1772, IEEE, Yokohama.

Montgomery, J. (1971), On the complete eigenvalue solution of ridged waveguide, *IEEE Trans. Microwave Theory Tech.*, *19*(6), 547–555, doi:10.1109/TMTT.1971.1127572.

Nicolson, A. M., and G. F. Ross (1970), Measurement of the intrinsic properties of materials by time-domain techniques, *IEEE Trans. Instrum. Meas.*, *19*(4), 377–382, doi:10.1109/TIM.1970.4313932.

Olmi, R., M. Bini, R. Nesti, G. Pelosi, and C. Riminesi (2004), Improvement of the permittivity measurement by a 3D full-wave analysis of a finite flanged coaxial probe, *J. Electromagn. Waves Appl.*, 217–232, doi:10.1163/156939304323062103.

Oppenheim, A. V., and R. W. Schafer (2010), *Discrete-Time Signal Processing* 3rd ed., Pearson Educ., Upper Saddle River, N. J.

Peterson, A. F., S. L. Ray, and R. Mittra (1998), *Computational Methods for Electromagnetics*, IEEE Press, New York.

Pyle, J. (1966), The cutoff wavelength of the TE_{10} mode in ridged rectangular waveguide of any aspect ratio, *IEEE Trans. Microwave Theory Tech.*, *14*(4), 175–183, doi:10.1109/TMTT.1966.1126212.

Sanadiki, B., and M. Mostafavi (1991), Inversion of inhomogeneous continuously varying dielectric profiles using open-ended waveguides, *IEEE Trans. Antennas Propag.*, *39*(2), 158–163, doi:10.1109/8.68177.

Seal, M. D., M. W. Hyde, and M. J. Havrilla (2012), Nondestructive complex permittivity and permeability extraction using a two-layer dual-waveguide probe measurement geometry, *PIER*, *123*, 123–142, doi:10.2528/PIER11111108.

Shin, D. H., and H. J. Eom (2003), Estimation of dielectric slab permittivity using a flared coaxial line, *Radio Sci.*, *38*(2), 1034, doi:10.1029/2002RS002776.

Stewart, J. W., and M. J. Havrilla (2006), Electromagnetic characterization of a magnetic material using an open-ended waveguide probe and a rigorous full-wave multimode model, *J. Electromagn. Waves Appl.*, *20*, 2037–2052, doi:10.1163/156939306779322693.

Sun, W., and C. Balanis (1993), MFIE analysis and design of ridged waveguides, *IEEE Trans. Microwave Theory*, *41*(11), 1965–1971, doi:10.1109/22.273423.

Tantot, O., M. Chatard-Moulin, and P. Guillon (1997), Measurement of complex permittivity and permeability and thickness of multilayered medium by an open-ended waveguide method, *IEEE Trans. Instrum. Meas.*, *46*(2), 519–522, doi:10.1109/19.571900.

Utsumi, Y. (1985), Variational analysis of ridged waveguide modes, *IEEE Trans. Microwave Theory Tech.*, *33*(2), 111–120, doi:10.1109/TMTT.1985.1132958.

Wang, S., M. Niu, and D. Xu (1998), A frequency-varying method for simultaneous measurement of complex permittivity and permeability with an open-ended coaxial probe, *IEEE Trans. Microwave Theory Tech.*, *46*(12), 2145–2147, doi:10.1109/22.739296.

Weir, W. B. (1974), Automatic measurement of complex dielectric constant and permeability at microwave frequencies, *Proc. IEEE*, *62*(1), 33–36, doi:10.1109/PROC.1974.9382.

Wexler, A. (1967), Solution of waveguide discontinuities by modal analysis, *IEEE Trans. Microwave Theory Tech.*, *15*(9), 508–517, doi:10.1109/TMTT.1967.1126521.

Wu, M., X. Yao, and L. Zhang (2000), An improved coaxial probe technique for measuring microwave permittivity of thin dielectric materials, *Meas. Sci. Technol.*, *11*(11), 1617–1622, doi:10.1088/0957-0233/11/11/311.